The Impact of Ground-Based Glaciogenic Seeding on Orographic Clouds and Precipitation: A Multisensor Case Study

BINOD POKHAREL, BART GEERTS, AND XIAOQIN JING

Department of Atmospheric Science, University of Wyoming, Laramie, Wyoming

(Manuscript received 17 September 2013, in final form 20 November 2013)

ABSTRACT

A case study is presented from the 2012 AgI Seeding Cloud Impact Investigation, an experiment conducted over the Sierra Madre in southern Wyoming to study the impact of ground-based glaciogenic seeding on precipitation. In this case, on 21 February, the temperature in the turbulent boundary layer above cloud base in the target region was just below −8°C, the target orographic clouds contained liquid water, and the storm was rather steady during the measurement period, consisting of an untreated period, followed by a treated period. Eight silver iodide (AgI) generators were used, located on the windward mountain slope. This study is unprecedented in its diversity of radar systems, which included the W-band (3 mm) profiling Wyoming Cloud Radar (WCR), a pair of Ka-band (1 cm) profiling Micro Rain Radars (MRRs), and an X-band (3 cm) scanning Doppler-on-Wheels (DOW) radar. The WCR was on board a research aircraft flying geographically fixed tracks, the DOW was located on the main mountain pass in the target region, one MRR was at this pass, and the other was upstream of the generators. Composite data from the three radars indicate that near-surface reflectivity was higher during seeding, a change that could not be accounted for by storm intensification upstream of the generators. Data from a Parsivel disdrometer at the pass indicate that the concentration of snow crystals of all sizes was larger during seeding, although this change was somewhat delayed. This study highlights the challenge of an observational study to unambiguously identify a seeding signal, as well as the value of cumulative corroborative evidence from independent sources.

1. Introduction

Water is vital for humanity and the environment. Water availability is limited yet demand is expected to continue to rise. Limited resources and increasing demand have prompted an interest in the feasibility of augmenting the water supply by means of cloud seeding. The most researched and widely practiced method of advertent weather modification aimed at precipitation enhancement in the western United States is the glaciogenic seeding of cold-season orographic clouds (e.g., Super and Boe 1988; Super and Heimbach 1988; Deshler et al. 1990; Holroyd et al. 1995; Super 1999; Huggins 2007).

Although weather modification research started in the 1940s, the impact of glaciogenic seeding remains uncertain because of the challenge of detecting a signal in the precipitation, which is an extremely noisy field in space and time (Garstang et al. 2005). The most recent research effort to shed light on the efficacy of ground-based silver iodide (AgI) seeding of orographic clouds is the Wyoming Weather Modification Pilot Project (WWMPP; Breed et al. 2014). A small field campaign, the 2012 AgI Seeding Cloud Impact Investigation (ASCII-12), was conducted over the Sierra Madre in southern Wyoming (Fig. 1) during January–March 2012 within the context of the multiyear WWMPP (Geerts et al. 2013). ASCII-12 was funded by the National Science Foundation with the specific aim to use new observational tools, such as a millimeter-wavelength profiling radar, to investigate cloud-microphysical changes in glaciogenic-seeded orographic clouds. The present paper is an observational case study, using a variety of data collected as part of the ASCII-12 campaign and the WWMPP.

Ground-based glaciogenic cloud seeding outcomes depend on several factors, in particular cloud temperature, cloud liquid water, and ice crystals from within (in situ ice nucleation), below (ground-based ice initiation), or above (seeder–feeder) the supercooled cloud. Temperature is a key parameter since the activation of AgI and natural ice nuclei and the rate of diffusional snow growth are temperature dependent. The temperature dependence of the ice-nucleating ability of AgI nuclei

Corresponding author address: Binod Pokharel, Dept. of Atmospheric Science, University of Wyoming, Laramie, WY 82071. E-mail: bpokhare@uwyo.edu

DOI: 10.1175/JAMC-D-13-0290.1

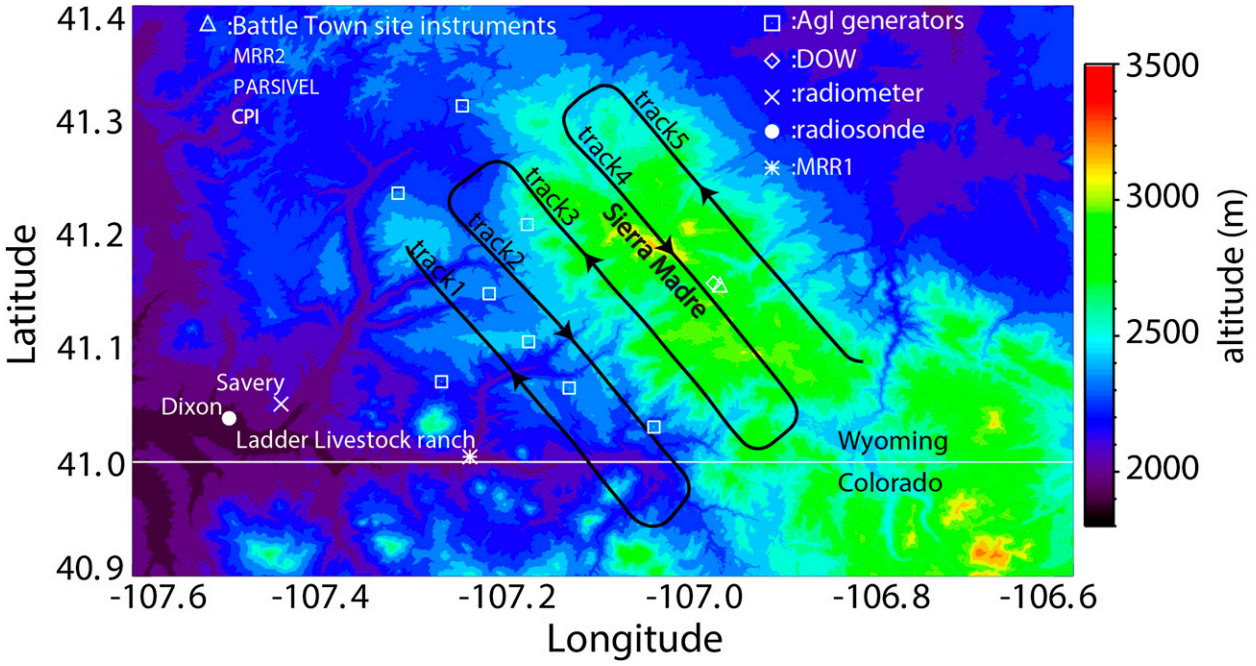

FIG. 1. ASCII-12 experimental design map, showing the UWKA ladder flight pattern (black line with arrows), the AgI generator locations, and ground-based instruments. The DOW and the Battle town site instruments are nearly collocated at Battle Pass. The terrain is shown in the background.

produced via combustion of an acetone solution from ground-based generators used in the WWMPP (Breed et al. 2014) is described in DeMott (1997). Liquid water content (LWC) and drop size distribution matter as well, although suitable ranges are poorly understood (Grant and Elliott 1974; Morrison et al. 2013). Numerical sensitivity analyses by Li and Pitter (1997) have shown that precipitation enhancement increases with cloud droplet concentration in the temperature range suitable for condensation freezing and contact freezing.

Winter orographic clouds are often remarkably shallow and much of the natural snow growth appears to occur within the turbulent boundary layer (BL) closely coupled to the underlying terrain (Geerts et al. 2011). Thus, ice crystal generation from the ground up must be considered (Rogers and Vali 1987; Vali et al. 2012). Two leading mechanisms are blowing snow, which is dependent on wind speed and snowpack surface conditions (Kristovich et al. 2012), and Hallett–Mossop-type ice multiplication on rimed surfaces such as trees, which is very temperature dependent and requires a threshold droplet size. Boundary layer turbulence in a water-saturated environment then can mix ice crystals from the ground into the lowest ~1 km above the terrain, where turbulent updrafts can enhance growth by diffusion or accretion (Geerts et al. 2011). Ice crystals can also be introduced into shallow orographic clouds from aloft (e.g., Saleeby et al. 2009). This mechanism (the seeder–feeder mechanism) can be evaluated readily with a sensitive profiling radar, unlike ground-based seeding, which is imperceptible in a precipitating orographic cloud. The ability of a mountain surface to naturally introduce ice crystals into orographic clouds is far more difficult to measure because the source ice crystals are small (and thus indistinguishable by radar in the presence of falling snow), in cloud (where a lidar signal attenuates quickly), and close to complex terrain. Yet its importance may be significant and underappreciated.

Thus, while glaciogenic seeding clearly triggers ice crystal formation in supercooled clouds (Schaefer 1946; Vonnegut 1947), both the impact of cloud seeding on precipitation and factors affecting orographic cloud seeding efficacy are difficult to measure. This explains why no more progress has been made in demonstrating the effectiveness of ground-based glaciogenic seeding. The latest report of the U.S. National Research Council on weather modification (NRC 2003) identified numerous challenges to demonstrating cloud seeding efficacy within the context of natural variability and recommended capitalizing on "new remote and *in-situ* observation tools" to remedy this situation. That precisely is the objective of this paper, by means of an ASCII-12 case study.

The experimental design employed in this paper is described in section 2. The reason why this case is chosen is explained in section 3. Data from three different radar systems are used in section 4 to document the impact of

seeding on radar reflectivity, a measure of precipitation rate. Changes in the snow size distribution at the surface are described in section 5. The findings are summarized in section 6.

2. Experimental design and instrumentation

The experimental design of the ASCII-12 campaign is described in Geerts et al. (2013). Here, we only discuss the instruments used in the present study, which focuses on the 21 February 2012 intensive observation period (IOP). The University of Wyoming King Air (UWKA) research aircraft carried several cloud and precipitation particle probes, but data collected at flight level are often of little use in detecting a seeding impact since ground-based generators were used, no convection was present, and the flight level remained above the turbulent BL: in this case the flight level was either 4.0 km above mean sea level (MSL) (~−13°C), which is 0.9 km above Battle Pass, or else 4.9 km MSL (~−16°C). The in situ measurements are still useful in characterizing the upper cloud region.

The UWKA was equipped with the profiling W-band (3-mm wavelength) Doppler Wyoming Cloud Radar (WCR) and the Wyoming Cloud Lidar (WCL) (Wang et al. 2012). Three WCR antennas were in operation, the nadir and zenith antennas (allowing profiling), and a slant-forward antenna (allowing dual-Doppler synthesis below flight level).

Eight AgI generators were distributed on the western (upwind) side of the mountain. Instruments on the ground were concentrated near Battle Pass, a Continental Divide pass (elevation 3034 m) in the Sierra Madre (Fig. 1). A scanning dual-polarization X-band (3 cm) Doppler-on-Wheels (DOW) radar was located on an exposed knoll at Battle Pass. The DOW conducted full volume scans every 8 min, alternating with a 1.5-min series of range–height indicator scans along the wind direction (forecast or sounding measured, at 700 hPa).

An elevated platform surrounded by trees, located some 500 m downwind of the DOW and referred to as the Battle town site, hosted a Micro Rain Radar (MRR) and several snow measuring instruments including a Yankee Hotplate, an ETI precipitation gauge, and a Parsivel disdrometer. An MRR is a low-power, frequency-modulated, continuous-wave (FM-CW) profiling Doppler radar operating in the Ka-band (24 GHz, or 1.2 cm). A second MRR was at the Ladder Livestock ranch location upstream of most AgI generators (Fig. 1).

The Parsivel disdrometer is an optical sensor with a laser diode that produces a horizontal sheet of light 30 mm wide, 180 mm long, and 1 mm high (Löffler-Mang and Joss 2000; Löffler-Mang and Blahak 2001; Yuter et al. 2006). The laser light is received at a photodiode that samples at 50 kHz. When particles pass through the light sheet, a portion of the transmitted laser light is blocked and the voltage produced by the photodiode is reduced. The amplitude of the voltage drop is related to the size of the particle and the duration of the voltage drop is related to the fall speed of the particle (Yuter et al. 2006). The instrument measures the maximum diameter of the 1D projection of the particle, which may be smaller than the actual maximum diameter. Vendor-supplied software computes the particle number concentration as a function of size and as a function of fall velocity (Yuter et al. 2006).

GPS Advanced Upper-Air Sounding (GAUS) rawinsondes were released from Dixon, upwind of the Sierra Madre. Rawinsondes were launched roughly every hour in this case to monitor the inflow humidity, stability, and wind profile. A passive microwave radiometer and an automated weather station operated near Dixon. This radiometer provides an integral estimate of the liquid water path (LWP) along a slant path toward the Sierra Madre at elevation angles of 8° and 12°, in order to capture the clouds over the mountain.

The ASCII-12 campaign was a physical (not randomized) experiment, focused not on surface snowfall amounts, but rather on cloud and precipitation changes above the surface. Experience had shown that detailed WCR transects of reflectivity at various distances downstream of AgI generators did not reveal any obvious reflectivity changes; therefore, any changes have to be analyzed in a composite sense (Geerts et al. 2010). The same experience also confirms the benefit of "control" (untreated) measurements upstream of AgI generators in order to quantify natural variations in vertical precipitation profiles. Therefore, the ASCII-12 experimental design included control measurements for all three radar systems. One of the MRRs was located ~10 km upstream of the most commonly used AgI generators, at the Ladder Livestock ranch, and the other ~20 km downwind of the generators at the Battle town site (Fig. 1). The DOW scanned not only the target region at close range, but also a more distant control region upstream of the generators, with a 0° beam reasonably close to the upstream terrain. Both the MRR pair and the DOW allow simultaneous comparisons between the control and target regions. Because the MRR vertical profiles represent a point on a map only, there must be evidence that the AgI nuclei plume from at least one of the generators advected over Battle Pass. We examine both the measured near-surface flow and silver in snow samples collected at the Battle town site.

A series of five geographically fixed aircraft tracks (the "ladder"; Fig. 1) was flown repeatedly. One of these

TABLE 1. Definition of NOSEED and SEED periods for the 21 Feb 2012 IOP. Eight AgI generators (Fig. 1) were in operation from 2120 to 0120 UTC ± a few minutes.

	NOSEED		SEED	
Instrument	Start (UTC)	Stop (UTC)	Start (UTC)	Stop (UTC)
UWKA	1957:05	2111:38	2143:43	2258:46
MRR*	1918:00	2139:00	2140:00	0138:00
DOW**	1916:51	2127:29	2127:45	0011:38
Parsivel	1918:00	2139:00	2140:00	0138:00

* One of the two MRRs (Battle Pass) was not operational during half of the SEED period (2213:00–0021:00 UTC).
** The DOW terminated operations at 0011:38 UTC.

flight tracks (labeled track 1 in Fig. 1) served as the control, being located upstream of the most commonly used AgI generators, and four flight tracks were downstream of the generators (tracks 2–5). The UWKA control–target comparisons were not truly simultaneous, unlike those of the DOW and MRRs. Also unlike the DOW and MRR, the UWKA control area (track 1) was not truly untreated, since one generator was on the upstream side of track 1 (Fig. 1). (In this case the low-level wind was from 250° to 260°.) Track 1 is a trade-off between representativeness (proximity to orographic forcing) and seeding impact assessment (target versus control). It may not be untreated, but it is less treated. The generator locations were chosen for the multiyear WWMPP. ASCII-12 was not at liberty to have the AgI generator west of track 1 switched off; as this would impact the integrity of the WWMPP randomized experiment.

Tracks 2 and 3 were located on the upwind side of the mountain crest. Track 4 roughly followed the Sierra Madre crest, and track 5 was in the lee. Two ladders were flown before AgI generators turned on (referred to hereinafter as NOSEED; Table 1) and two ladders were flown while the AgI generators were in operation (referred to as SEED). The aircraft's NOSEED and SEED periods thus were equally long, but lasted only ~100 min. The aircraft's endurance constrained it from flying more than four ladder patterns. The WCR has fixed antennas pointing down and up from the aircraft and the nadir view provides radar data within ~30 m of the ground, which is the prime location from which to see the seeding signature.

The AgI generators were on for 4 h in the case examined here; thus, the NOSEED and SEED periods for the ground-based measurements were longer (Table 1). A lag of 20 min is assumed for the start of the SEED period at Battle Pass, to account for advection from the AgI generators. A representative advection speed was estimated from the mean GAUS wind vector between the surface and the Battle Pass level (~700 hPa).

The three radar systems (WCR, the MRR pair, and DOW) are fully complementary in their evaluation of the seeding effect. They operate at different frequencies, have different viewing–scanning strategies and resolutions, and their SEED–NOSEED periods are different in this case (Table 1). Each system has certain strengths and weaknesses; for example, WCR data extend very close to the ground but offer less time continuity.

3. Ambient conditions and cloud characteristics

a. *Ambient conditions*

The 21 February 2012 IOP is selected for this case study because seeding conditions likely were favorable, and because the storm was relatively steady during the IOP. A broad upper-level trough was present over the Great Plains, and a low-level low pressure system in the northern Great Plains resulted in strong westerly flow over Wyoming's high terrain. An anticyclonic jet streak approached Wyoming from the northwest. Satellite imagery indicates widespread snow cover upstream of the Sierra Madre, low-level orographic clouds over the Sierra Madre and adjacent mountain ranges, and upper-level cloud spreading from the northwest. Light and occasionally moderate precipitation continuously fell over the mountain during the IOP, but not in the surrounding valleys.

Three soundings were collected during this IOP, two of which are shown in Fig. 2: one during NOSEED and one during SEED. The northwesterly wind aloft is evident, as well as veering flow (warm-air advection) mainly between the surface and 600 hPa. An unsaturated stable layer was building into an inversion between 630 and 580 hPa (its base a few hundred meters above the Sierra Madre peak), and this trapped the orographic cloud below. The low-level cloud was coupled with the surface, yet the cloud base appeared to be rather high: the mixed-layer lifting condensation level (LCL) was 2950 m MSL, or just ~70 m below the Battle Pass level. An ~1-km-deep cloud layer persisted below the inversion over Dixon during the IOP; WCR and DOW data indicate occasional light snowfall from levels above the inversion, with echo tops near −22°C.

b. *Cloud properties*

This is the only case in ASCII-12 measurements with substantial LWP (>0.2 mm, measured by the radiometer near Dixon) and rather low cloud-base temperatures (about −8°C, according to the soundings). This matters because both observational and laboratory studies show that the effectiveness of AgI seeding to augment precipitation depends on temperature and the presence of

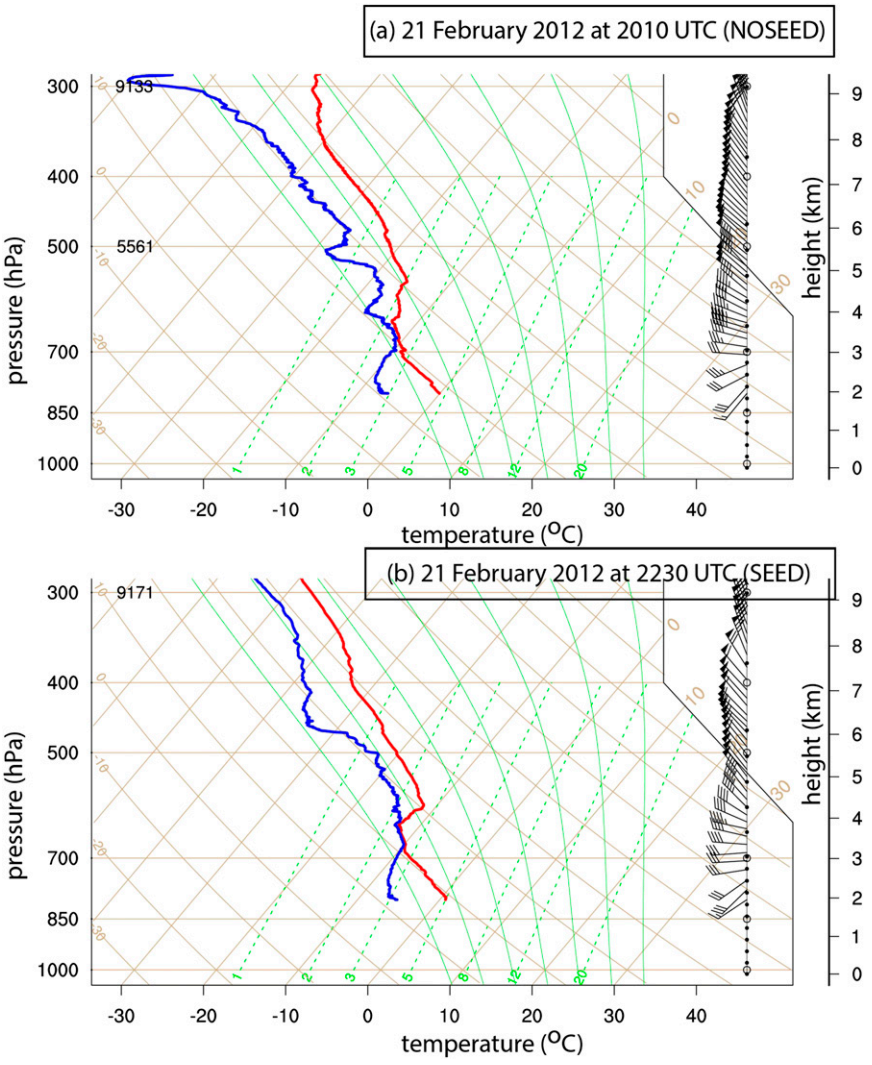

FIG. 2. Skew T–log$p$ display of rawinsonde data from Dixon during the (a) NOSEED period (2110 UTC) and (b) SEED period (2230 UTC). A full barb = 5 m s^{-1} (~10 kt; 1 kt = 0.51 m s^{-1}).

supercooled liquid water (SLW) (Grant and Elliott 1974; Li and Pitter 1997; Givati and Rosenfeld 2005; Zipori et al. 2012). A cloud-base temperature significantly above −8°C, and limited vertical mixing in cloud, may render AgI seeding ineffective, as the AgI activation (measured as the number of crystals yielded per gram of AgI) decreases by 2.5 orders of magnitude between −10° and −6°C (DeMott 1997). The DeMott (1997) study refers to aerosols generated using airborne wingtip burners, but its results can be generalized to ground-based burners used in the WWMPP, as the AgI solution vaporized in the WWMPP burners is the same as the one tested in DeMott (1997) (Super et al. 2010).

The presence and abundance of SLW was estimated not only using the radiometer, but also using flight-level liquid water probes. The initial flight level was 13 kft MSL (4.0 km), but the aircraft experienced ice buildup on the exposed probes and on the airframe due to the abundance of SLW. Thus, upon completion of the first ladder, the flight level was increased to 16 kft (4.9 km). In short, the cloud conditions appeared suitable for glaciogenic seeding. It is quite possible of course that the AgI nuclei injection was overwhelmed by natural seeding during this IOP, either from aloft (seeder–feeder), as cloud tops were as cold as −22°C, or from the surface, as the wind was strong and widespread fresh snow was present; that is, blowing snow could be mixed into the cloudy turbulent BL (Kristovich et al. 2012). These ice crystal sources are difficult to quantify, but a qualitative assessment is possible by examining the WCR and WCL transects for an along-wind flight leg flown in the middle of this IOP, after the completion of two NOSEED

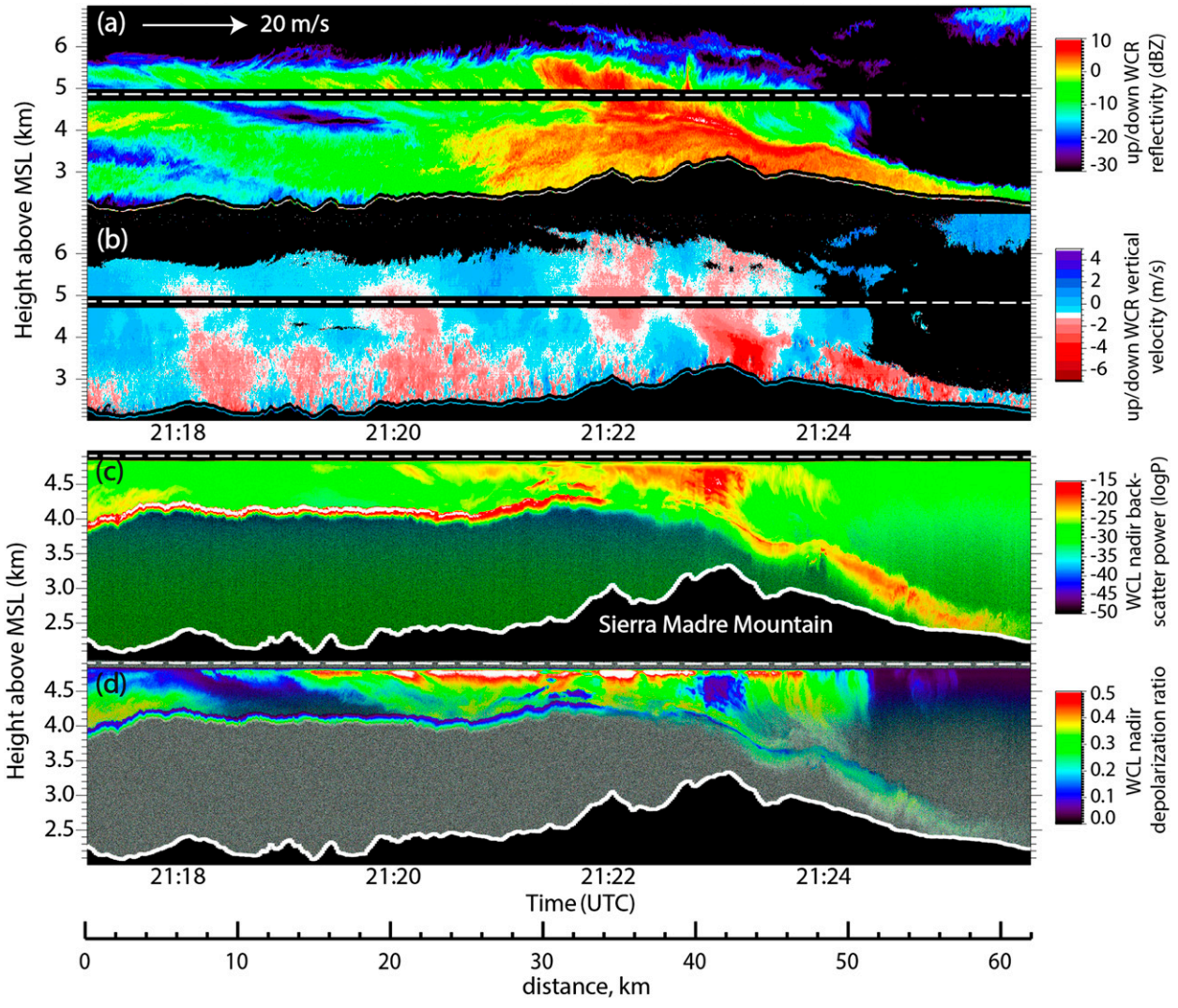

FIG. 3. WCR and WCL transect for the along-wind (260° → 80°) flight leg over the Sierra Madre on 21 Feb 2012. The wind direction is from left (west) to right (east). The dashed white line in all panels is the UWKA flight level. The black belt around this line in the top two panels is the radar blind zone for the zenith and nadir WCR antennas. The terrain profile can be seen in all panels. (a) WCR radar reflectivity and (b) WCR hydrometeor vertical velocity (both above and below the aircraft); (c) WCL backscatter power and (d) WCL depolarization ratio (both below the aircraft only).

ladders but before the first AgI plumes could have reached the mountaintop (Fig. 3).

Snow was present aloft, between 5 and 6 km MSL, from the upwind margin near Dixon (left side of Fig. 3a) to the mountaintop. Radar and lidar transects clearly show the deep plunging flow on the lee side of the mountaintop. The rapid and complete attenuation of lidar backscatter power (Fig. 3c) and low depolarization ratio (Fig. 3d) at about 4.0 km MSL on the upwind side indicate a well-defined liquid water cloud top. This liquid water cloud top vanishes in the lee, due to subsidence (Huggins 1995). The cloud layer between this liquid water top and the echo top (i.e., between 4 and 6 km MSL) consisted almost exclusively of ice particles (LWC $< 0.1\,\mathrm{g\,m^{-3}}$) according to the in situ probe that remained uncovered by ice (a hot-wire probe) and the WCL, which registered low backscatter power yet a high depolarization ratio in this layer. This upper snow layer could have acted as a source of ice crystals to the cloud below.

The WCR vertical velocity profile (Fig. 3b) reveals both terrain-driven eddies (ascent on the upwind side, descent on the lee side of local terrain features) and, in the lowest ~500 m AGL, finescale turbulent vertical velocity variations. This is the well-mixed BL driven by shear instabilities given the strong low-level wind (Geerts et al. 2011). An analysis of the WCR vertical

velocity along the ladder tracks shows that the turbulent BL is shallower along tracks 4 and 5 (Fig. 1), and deeper (up to 1000 m deep) along tracks 1–3; especially along their northwest side. Note the vertical velocity color key bar in Fig. 3b: it is centered at $-1\,\mathrm{m\,s^{-1}}$ to account for the typical fall speed of snow. Thus, the blue (red) areas in Fig. 3b can be interpreted as updrafts (downdrafts), without bias.

Blowing snow crystals can be mixed into this BL, which extends above the cloud base (~3 km MSL) over the higher terrain, between $x \sim 20$ km and mountaintop (and into the lee). Clearly, much of the low-level snow growth occurs between $x \sim 20$ km and mountaintop (Fig. 3a). WCR dual-Doppler vectors of hydrometeor motion in the plane of the transect in Fig. 3 (not shown) are inconclusive about the possibility of ground-based natural seeding: the dual-Doppler hydrometeor streamlines generally point toward the terrain in the upwind BL, but small, broken ice crystals lofted from the surface probably have a negligible fall speed, unlike the larger hydrometeors captured by radar.

c. *Natural variability*

To isolate the seeding impact, it is important that ambient conditions and storm structure are relatively steady during the IOP, even if "control" (untreated) radar data are available during SEED. The natural variability of precipitation is the main challenge in seeding impact detection (Garstang et al. 2005; Geerts et al. 2013). The timeline of ambient and cloud–precipitation structure parameters for this IOP is shown in Fig. 4. Data sources include soundings, WCR, surface stations, Geostationary Operational Environmental Satellites (GOES), and the upwind microwave radiometer. As expected from the warm-air advection wind profile in the soundings (Fig. 2), the 700-hPa temperature steadily increased (Fig. 4b), and so did the precipitable water (vertically integrated water vapor) (Fig. 4c), but the changes over 3 h are rather small (1 K and 12%, respectively). Other parameters do not show a clear trend. The low-level wind speed and direction impinging on the mountain and through Battle Pass were remarkably steady (Fig. 4a). The bulk Brunt–Väisälä frequency N (Fig. 4d) is calculated as the weighted mean of the dry value below the LCL and the moist value between the LCL and mountaintop level. It remains around $0.065\,\mathrm{s^{-1}}$, indicating that the lower-tropospheric stability was low, but not low enough to allow convection. (There was no potential instability.) The surface-to-mountaintop Froude number (Fr) was larger than 1 from all three soundings, suggesting ready transport of the upwind low-level air mass over the mountain, without blocking. The average LWP measured by the Dixon radiometer (Fig. 4e) was quite large (0.22 mm) and slightly higher during SEED than NOSEED (Fig. 4e). However, no change in LCL, calculated from the soundings and the Dixon surface station, was apparent during the IOP (Fig. 4e). The WCR mean echo top and mean near-surface reflectivity along track 1 (upwind of seven generators) increases first and then decreases during SEED (Fig. 4f). The GOES infrared temperature remained quite low, −35° to −40°C, suggesting the presence of cirrus near 8 km MSL (Fig. 4c). The WCR's up antenna reveals patchy cirrus clouds near 8 km MSL; some patches have fall streaks, but these evaporate before reaching the lower clouds (not shown). Overall, the 21 February storm and its ambient conditions were relatively steady during the IOP.

4. Radar detection of seeding impact

In a mixed-phase cloud with very low snow concentrations, radar reflectivity is dominated by the snow crystals and not the cloud droplets, even at W band. In fact, radar reflectivity is a good surrogate measure of snow mass and snowfall rate, as demonstrated by many published experimental studies not only for nonattenuating (centimeter wave) radars (e.g., Matrosov et al. 2009) but also for millimeter-wave radars (Matrosov 2007; Geerts et al. 2010; Pokharel and Vali 2011).

a. *WCR data*

The four WCR reflectivity transects collected along flight track 4 are shown in Fig. 5. Track 4 approximately aligns with the crest of the Sierra Madre range (Fig. 1). The flow is highly sheared (Fig. 2), about $20\,\mathrm{m\,s^{-1}}$ from the surface to storm top, as shown in the inset wind profiles in Fig. 5. In the northwest–southeast transect of track 4, the impact of this shear is evident as highly tilted precipitation features. The flow is mainly out of the page, however, across the crest. This cross-mountain flow starts to plunge upwind of the crest (Fig. 3a). A most obvious illustration of the profound impact of the mountain on this storm is the fact that the mean echo top for all four ladders steadily lowers from track 2 at 3.6 km AGL, to track 5 at merely 0.9 km AGL. The flow is mostly subsident along track 4 according to WCR vertical velocity transects (not shown), consistent with Fig. 3b. Yet this subsidence is too young along track 4 to evaporate the supercooled cloud water: the airborne backscatter lidar (WCL) indicates a well-defined liquid water cloud top persisting along track 4, for all four passes, near an altitude of 3.9–4.0 km MSL. The flight-level hot-wire probe (unaffected by icing) shows a rather high liquid water content ($\sim 0.3\,\mathrm{g\,kg^{-1}}$) in sections where this cloud is penetrated along track 4.

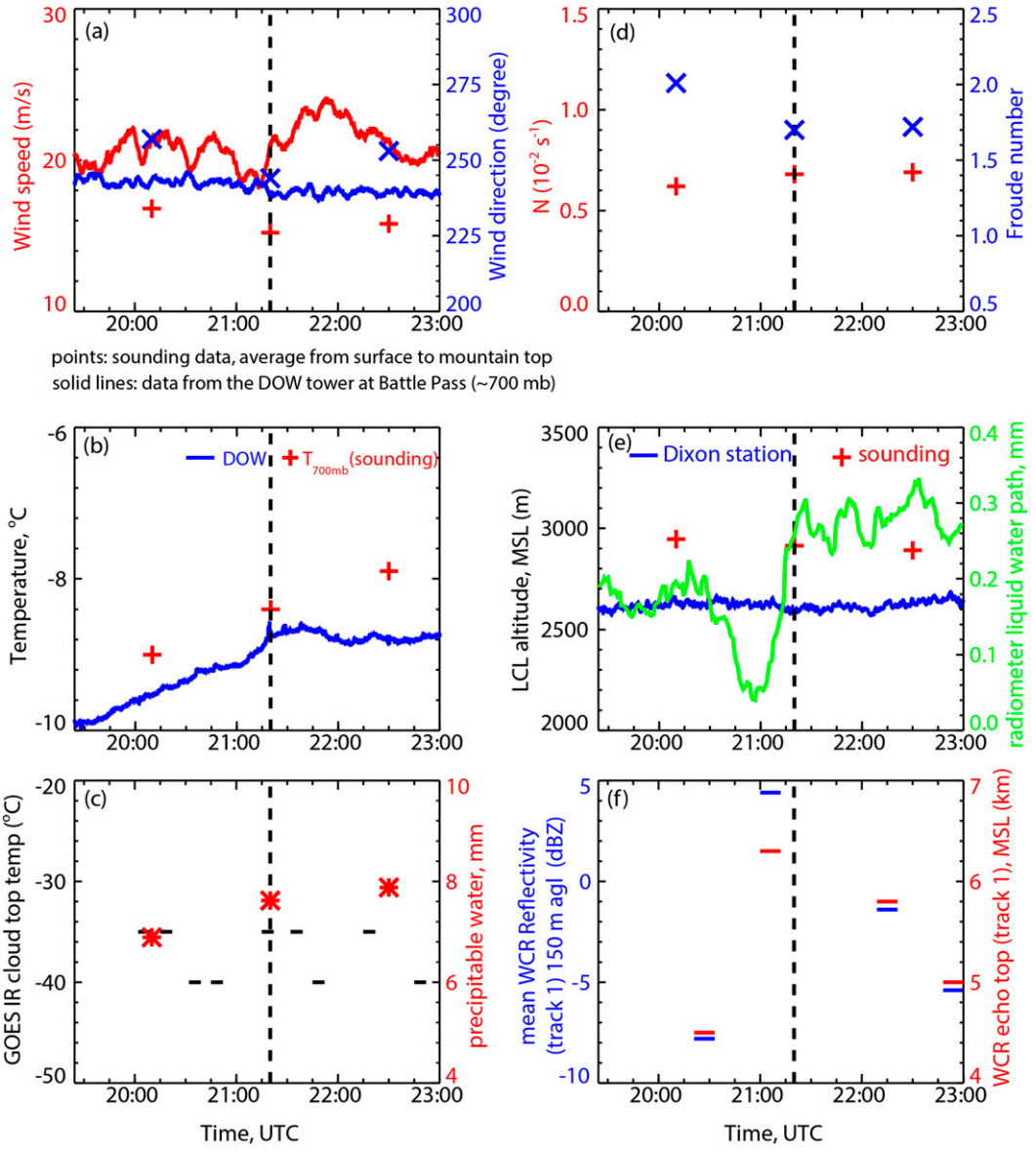

FIG. 4. Evolution of several atmospheric parameters during the course of the IOP on 21 Feb 2012, as measured by rawinsondes, weather stations in the upwind valley and on the mountain, WCR, and GOES. The vertical dashed line in all panels shows the activation time of the AgI generators.

Thus, the storm was shallow along track 4, often just 1 km deep between the LCL and the echo top. The precipitation structure was also quite steady during the IOP, an important argument in the selection of this case study. Light snowfall fell across the entire transect during all four passes. And the storm depth and average reflectivity did not change much, except for the third pass, when the storm was deeper and more intense.

The top two panels in Fig. 5 are during NOSEED and the bottom two panels are during SEED. The storm was more intense during the third pass, but this intensification is not sustained into the fourth and last pass, and is not concentrated within the BL (500–1000 m deep), where such would be expected for ground-based seeding. Also, it is not limited to the center and right sides of the transect, where most AgI plumes are believed to intersect this transect. The estimated upwind location of all operating AgI generators is shown in Fig. 5c, together with the estimated distance between the generators and the intersection with track 4. This assumes the average GAUS wind vector from the surface to mountaintop level. One may expect enhanced reflectivity downwind of the active AgI generators, in an area that expands with distance

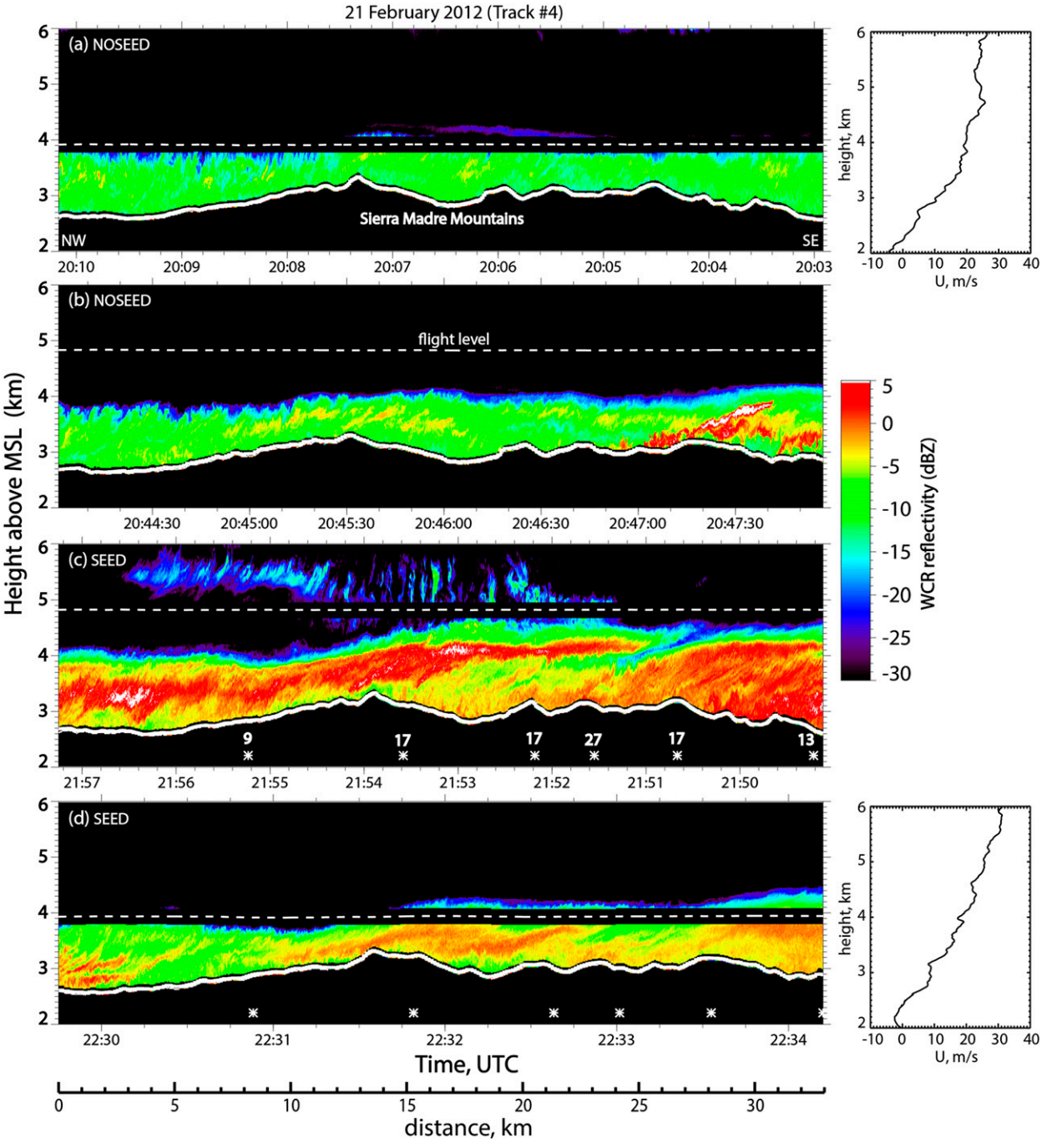

FIG. 5. Example UWKA radar reflectivity transects, collected along flight track 4 (Fig. 1) on 21 Feb 2012: (a),(b) NOSEED period and (c),(d) SEED period. The low-level wind is mainly into the page, but the wind shear vector points from left (NW) to right (SE) along these transects, according to the Dixon sounding wind profiles at matching times, as shown in two insert images on the right (U = along-transect wind, along 322°, positive from the NW). The star symbols at the bottoms in (c),(d) indicate the locations along the x axis of the projection of six AgI generators into this transect, and the numbers next to these stars in (c) are the fetch (km) between the generators and the transect.

from the generators. No well-defined plumes of enhanced reflectivity can be seen along the projected AgI plume locations in the third and fourth transects (Figs. 5c,d); in other words, the seeding impact is not obvious in the W-band reflectivity transects.

Therefore, the WCR reflectivity data are composited for all flight sections downwind of AgI generators in frequency-by-altitude diagrams (FADs; Yuter and Houze 1995). The diagrams shown in Fig. 6 display the normalized frequency of reflectivity as a function of height AGL. The ground is chosen as reference height because the AgI generators are located at various elevations on the ground, and because to a first order the BL and isentropes follow the terrain. These FADs show distributions of reflectivity values at any height, and because they are not normalized level by level, they also show the relative frequency of echoes at various levels. Thus, the frequencies shown across the entire FAD domain add up to unity. This implies that point-by-point differences can be taken between two 2D distributions (e.g., SEED minus NOSEED), even when the absolute frequencies are different.

The WCR reflectivity FADs composited from all downwind (treated) tracks (2–5) during NOSEED and SEED are shown in Figs. 6a and 6b, respectively. These FADs confirm that clouds were shallow during both periods, and the echoes quite weak. The average reflectivity of ~0 dBZ near the surface corresponds to a snowfall rate of only ~1 mm h^{-1} (Fig. 6c). Three differences are apparent: first, the upper-level (2.5–4.5 km AGL) echo seen in Fig. 3 was more common early in the IOP (NOSEED) and essentially vanished during SEED (Figs. 6a,b). Next, the shallow orographic echoes were deeper during SEED, and third, high radar reflectivity values (>−5 dBZ) were more common near the surface during SEED.

These differences are more apparent in the normalized frequency *difference* FAD (Fig. 6c). A strong frequency dipole is found near the surface, with more common occurrences of high-reflectivity values during SEED, at the expense of the frequency of low-reflectivity values. This dipole quickly weakens with height in the lowest 500 m, the depth of the well-mixed layer. Correspondingly, the average reflectivity value (black lines in Fig. 6c) is higher during SEED at low levels. (The difference in mean value, SEED minus NOSEED, is positive and large also at midlevels, between 0.7 and 1.7 km AGL, but is not significant given the low frequency of echoes there.) This positive change of low-level radar reflectivity may not be due to AgI seeding: natural variability over this rather short span of time cannot be ruled out. The relative change is rather large: the mean snowfall rate during SEED is almost twice as large as during NOSEED (Fig. 6c).

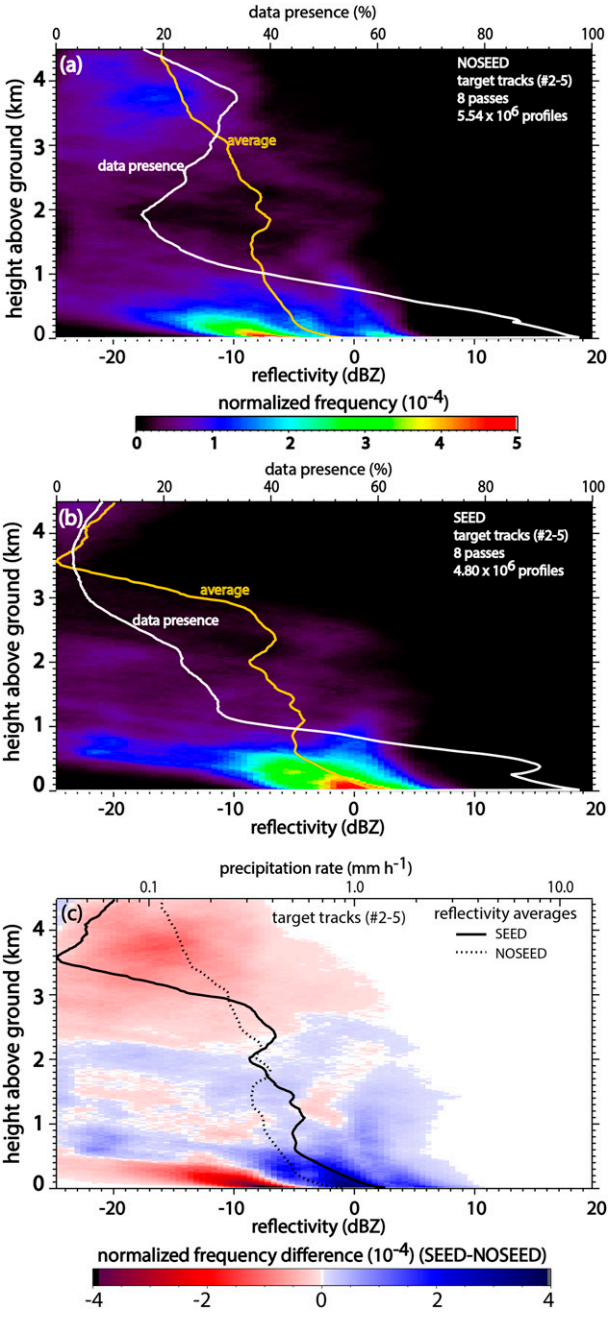

FIG. 6. Normalized FAD diagrams of WCR reflectivity Z for the flight on 21 Feb 2012 for the four tracks downwind of the AgI generators (target region): (a) NOSEED and (b) SEED periods, and (c) their difference. Also shown are the mean reflectivity profiles [orange lines in (a) and (b) and black lines in (c)] and the "data presence," i.e., the percentage of WCR range gates with radar echo as a function of height [white line in (a) and (b)]. The precipitation rate R shown in the upper abscissa of (c) is inferred from $R = 0.39Z^{0.58}$ (Pokharel and Vali 2011).

Natural variability over the mountain area (tracks 2–5) remains unknown, but it can be estimated from changes across track 1 between the two periods, assuming that (i) natural changes are spatially rather uniform, (ii) the effects of one AgI generator upwind of track 1 can be ignored, and (iii) short-term local variability within either period is small. The last assumption matters because there are only two track-1 passes during SEED and NOSEED: a two-transect average for a field of small convective cells, for instance, will be highly variable depending on the exact timing of the transects. This assumption does seem to apply because DOW surveillance scans show rather uniform echoes across the domain during the IOP (no convective cells).

The track-1 reflectivity FADs composited during NOSEED and SEED are shown in Figs. 7a and 7b, respectively. The changes aloft are similar to those for tracks 2–5 (Fig. 6): the echoes tend to become shallower during SEED, with just some decoupled, weak upper-level echoes remaining. But snowfall is clearly weakening in the BL along track 1. This dramatic change at low levels is evident in the difference FAD (Fig. 7c). The low-level dipole is opposite that observed over the treated tracks. Yet snowfall remains widespread during SEED along track 1. (The data presence is 100% in the BL in Fig. 7b.) This adds confidence that the positive low-level change over the downstream tracks (Fig. 6c) is attributable to AgI seeding.

To further analyze the possible seeding effect, we compare the reflectivity difference FADs for the two target tracks (2 and 3) closer to the generators (Fig. 8a) to that for the two more remote target tracks (4 and 5), that is, those near the mountain crest or in the lee (Fig. 8b). This reveals that the seeding effect appears to be stronger at longer fetch (Fig. 8b), where the near-surface dipole is better defined and the mean reflectivity difference is larger. This is promising for the MRR analysis (section 4b), because the downstream MRR was located between tracks 4 and 5 (Fig. 1). This apparent fetch effect may in fact be due to the dispersive widening of the plumes of AgI impact with fetch from the generators: along the short-fetch tracks, the WCR mostly samples unaffected cloud on the side of the (still narrow) AgI plumes (Fig. 1).

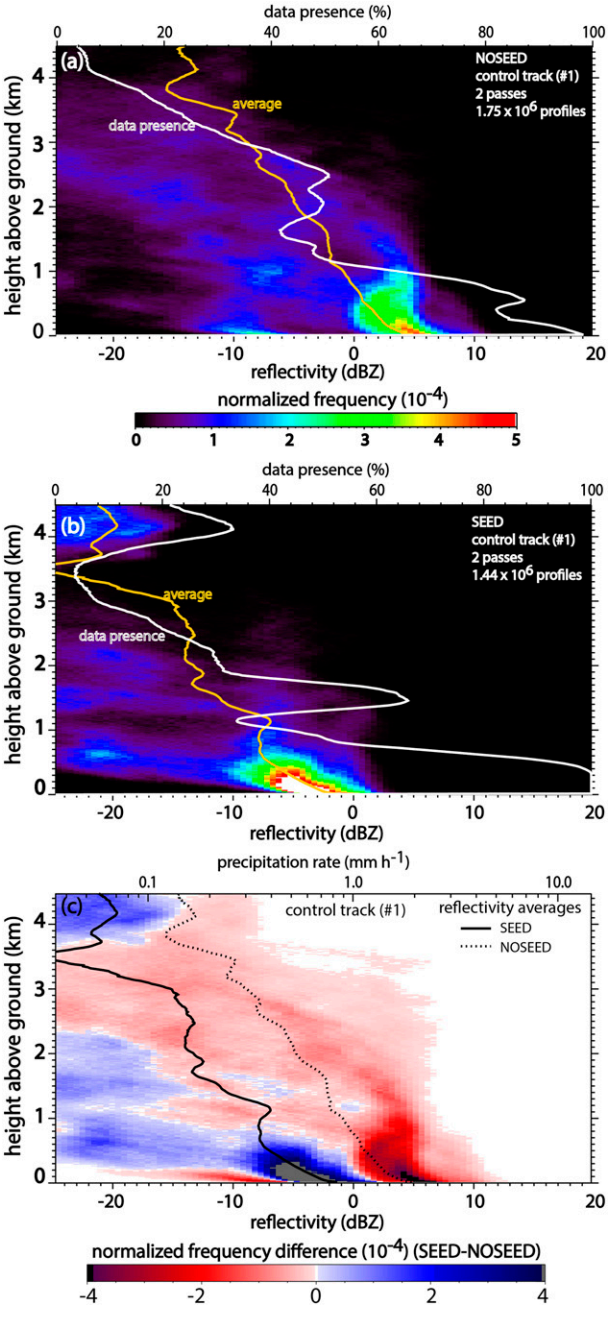

FIG. 7. As in Fig. 6, but the FADs apply to the flight track upwind of the AgI generators (control region).

b. MRR data

We are moderately confident that AgI plumes from at least one generator reached the Battle town site during SEED. This is based on the sounding wind profile (Fig. 2b) and the surface wind data at Dixon and at Battle Pass. A broad array of wind directions between 240° and 270° all suggest that at least one conical plume emerging from the AgI generators intercepts Battle Pass. This applies to cones at least 6° wide on either side of the wind direction. Under strong wind and some stratification, the AgI dispersion plumes may be closer to ±10°-wide cones, according to observational (Holroyd et al. 1988) and modeling (Chu et al. 2014, manuscript submitted to *J. Appl. Meteor. Climatol.*) studies. Yet snow chemistry analysis from three samples collected at the Battle town site is inconclusive. Each sample contained fresh snowfall

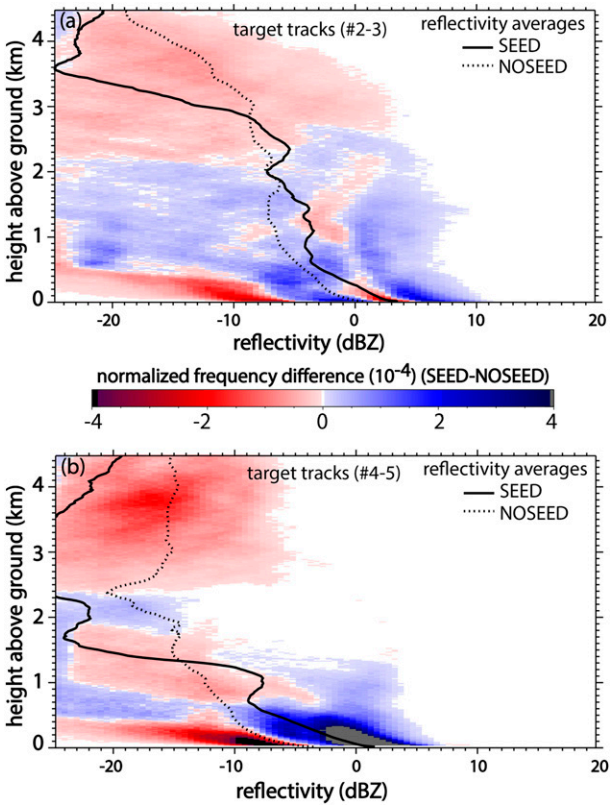

FIG. 8. Difference in normalized FAD (SEED − NOSEED) for WCR reflectivity for (a) the two target tracks just downwind of the generators (tracks 2 and 3) and (b) the two more distant flight tracks (4 and 5).

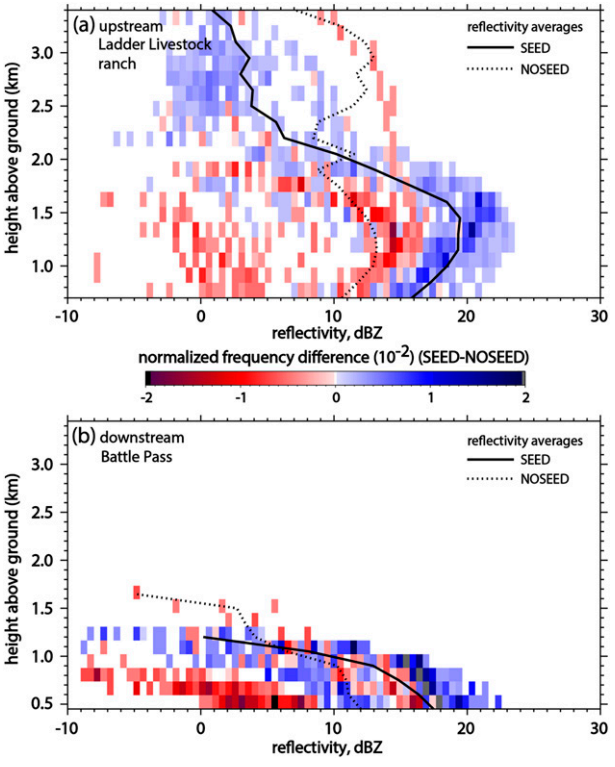

FIG. 9. Difference in normalized FAD (SEED − NOSEED) for (a) the upstream MRR (control) and (b) the downstream MRR (target). The NOSEED and SEED periods are defined in Table 1.

collected over ~30 min; one sample was during MRR NOSEED, the second straddled the NOSEED-SEED boundary (Table 1), and the third was early during SEED. This third sample does not show an elevated Ag concentration, and the measured Ag concentration is about what can be expected naturally, given the concentration of other trace elements (cerium and rubidium). Unfortunately, no other snow samples were collected during the remainder of the MRR SEED.

The first two range gates of the MRRs are excluded because they are too noisy, according to a test proposed by Maahn and Kollias (2012). This (together with the radar blind zone) implies that an effective lowest level of good data is 700 m (450 m) AGL for the upstream (downstream) MRR, whose gate spacing was set at 200 m (150 m). The WCR analysis (section 4a) suggests that this may be too high for most of the ground-based AgI seeding impact. The MRR NOSEED period is 2.5 h, ending with the estimated arrival time of the AgI plume at the Battle town site (Table 1). The NOSEED period does not start earlier because it would interfere with another AgI seeding event that ended 4 h before the seeding for the present case study. The SEED period is longer in principle, as AgI seeding was conducted for 4 h, but the downstream MRR was not operational during half of that time.

The difference FAD for the MRR reflectivity composited during SEED and NOSEED is shown in Fig. 9. The MRRs lack the power and sensitivity of the DOW and WCR; thus, the profile data are averaged over 1-min intervals, resulting in rather sparse FADs. The FAD differences confirm that the echoes are deeper upwind of the mountain than over the crest. The downstream MRR reflectivity increases in the lowest 1 km during SEED (Fig. 9b). The average increase is ~4 dBZ at the lowest MRR level, consistent with WCR-based findings (Fig. 8b). But a low-level increase between NOSEED and SEED periods is found above the Ladder Livestock ranch upstream of the AgI generators (Fig. 9a), which disagrees with the WCR-based finding (Fig. 7c). (At upper levels, the control MRR and WCR track 1 data do agree.) The downstream MRR is very close to the UWKA tracks (<1 km from track 4) but the upstream MRR is not (~6 km from track 1) (Fig. 1). This demonstrates the possibility of significant small-scale variations, in this case between the control MRR and the control

flight track. The discordant trend may be due also to the nonsimultaneity of the WCR and MRR SEED–NOSEED periods (Table 1).

In short, the target MRR was in a good location to be exposed to the impact of AgI seeding. The FAD differences in MRR reflectivity suggest a positive seeding effect, although it is rather small when taking upstream variability into account.

c. *DOW data*

The DOW radar completed full volume scans[1] to a maximum range of 48 km at 60-m-range resolution. This offers the advantage of rather large areas, sampled at rather high frequency (10-min intervals), compared to the MRR and WCR profile measurements. But the vertical resolution of a scanning ground-based radar becomes rather poor at range, even though the DOW's beamwidth is rather narrow (0.93°). Also, the base-elevation data are well above the ground in most areas since the DOW is located on a mountain pass. The lowest level AGL of DOW data are shown in Fig. 10. The lowest-elevation angle (0°) is unblocked in a narrow window to the west and a broader one to the east. Battle Pass is surrounded by higher terrain to the NW and the SE, and this terrain is cleared by DOW elevation angles above 3° and 6°, respectively. Therefore, the lowest unblocked DOW beam is quite high above the ground in these sectors. Fortunately, we are mostly interested in the western and eastern windows.

We define three areas of DOW volume data (Fig. 10). The control area is defined as a region mostly upstream of the AgI generators where the lowest unblocked DOW beam is no more than 1 km above the terrain. (There are three generators near the edges of the control area, but it is unlikely that their AgI impact plumes can reach the DOW volume, as they are ~600 m below the lowest DOW beam.) The upwind target area is downstream from most AgI generators, but upstream from the mountain crest (the Continental Divide). And the lee target area is downstream of the generators and the mountain crest. Both target areas further are delineated by the requirement that the lowest unblocked DOW beam cannot exceed 1 km AGL. It is useful to separate the seeding impact on opposite sides of the mountain, because it allows an assessment of fetch (similar to the comparison of WCR data from tracks 2 and 3 versus tracks 4 and 5; Fig. 8), and because the two sides are in different river basins, separated by the Continental Divide.

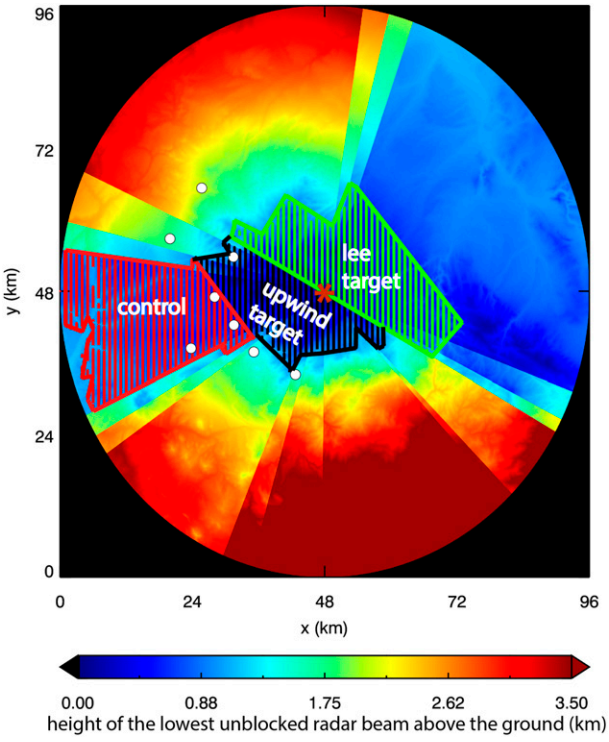

FIG. 10. Height (km AGL) of the lowest unblocked beam from the DOW radar, located at Battle Pass (Fig. 1). The DOW elevation angles used here range from 0° to 6° in 1° intervals. Also shown are three vertically hatched regions used in the analysis of the seeding impact: the control region (red), the upwind target region (black) upwind of the mountain crest, and the lee target region (light green) in the lee. The red asterisk shows the DOW location, and white circles are for the AgI generators.

The DOW spherical coordinate data (range, azimuth, and elevation) were thresholded to remove range-dependent noise and ground clutter and, then, were converted to a Cartesian grid with resolution (1000, 1000, 100 m) in the zonal, meridional, and vertical directions, using a Cressman weighting scheme with radii of influence (1000, 1000, 200 m) in the three dimensions.

The resulting FAD differences in DOW reflectivity during the NOSEED and SEED periods (Table 1) are shown in Figs. 11a–c for the three regions. There are no DOW data at lower altitude AGL in the control region, below ~500 m, because the control area is in the western foothills below Battle Pass. The storm intensity decreases between the two periods in the control region, consistent with the WCR analysis (Fig. 7c). Yet low-level DOW reflectivity increases in both target areas during SEED (Figs. 11b,c), which suggests a positive seeding effect, consistent with WCR and MRR analyses. Figure 11 also confirms that the storm depth decreases between the two periods, in all three regions.

[1] The volume coverage pattern was as follows: every 1° between 0° and 20° elevation, every 2° between 20° and 30° elevation, and every 4° between 30° and 70° elevation.

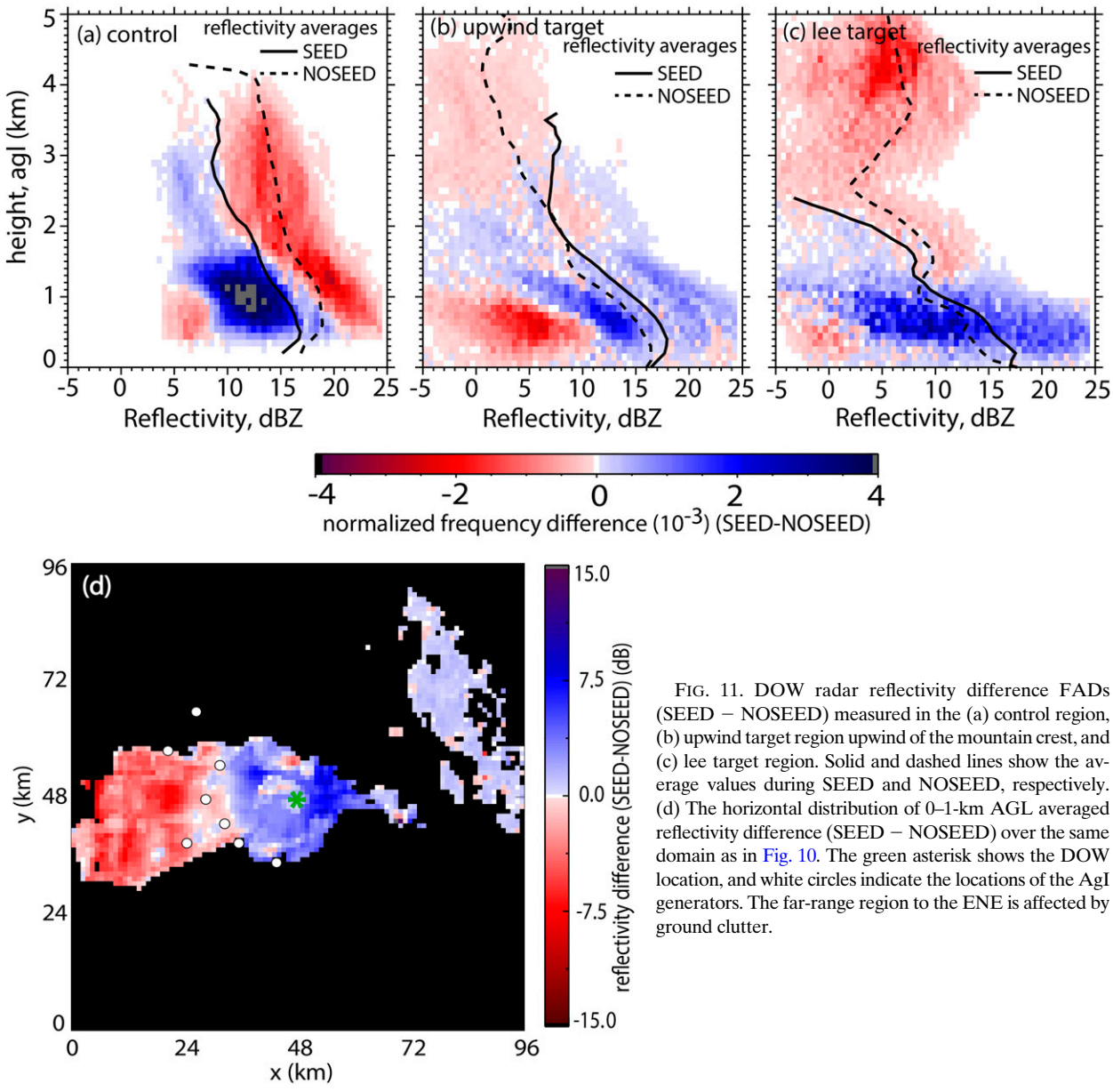

FIG. 11. DOW radar reflectivity difference FADs (SEED − NOSEED) measured in the (a) control region, (b) upwind target region upwind of the mountain crest, and (c) lee target region. Solid and dashed lines show the average values during SEED and NOSEED, respectively. (d) The horizontal distribution of 0–1-km AGL averaged reflectivity difference (SEED − NOSEED) over the same domain as in Fig. 10. The green asterisk shows the DOW location, and white circles indicate the locations of the AgI generators. The far-range region to the ENE is affected by ground clutter.

The difference between the two target areas is rather small. The low-level intensification during SEED is slightly stronger in the lee of the mountain, which is also consistent with the WCR measurements (Fig. 8). The surface to 1.0 km AGL averaged reflectivity difference (SEED-NOSEED) is mapped out in Fig. 11d. The near-surface snowfall intensity decreases in the region upwind of the AgI generators, yet it increases immediately downwind of the generators. There is even some suggestion of plumes of enhanced reflectivity emerging to the east of the southernmost three or four generators.

d. Seeding impact analysis: Radar data summary

The difference in the reflectivity vertical structures between two periods is largely due to natural storm variability, even in a rather steady storm like the one analyzed here. Some of the natural trend can be removed by considering the nearby trend over the same time, in an untreated area. We define the radar reflectivity impact parameter (ZIP) as the difference between the downstream (treated/target) average reflectivity change (SEED − NOSEED) and that upwind of the AgI generators (untreated/control). is calculated as

$$\mathrm{ZIP} = \Delta\mathrm{dB}Z_T - \Delta\mathrm{dB}Z_U, \quad (1)$$

where $\Delta\mathrm{dB}Z = \mathrm{dB}Z_S - \mathrm{dB}Z_N$ and subscript S (N) refers to SEED (NOSEED) while subscript T (U) refers to treated (untreated).

Given that reflectivity Z ($\mathrm{mm}^6\,\mathrm{m}^{-3}$) correlates rather well with precipitation rate R ($\mathrm{mm\,h}^{-1}$) at all three radar frequencies, and given our interest in the impact of glaciogenic seeding on R, we derive another parameter, the precipitation impact factor (PIF), which is defined as a relative change in R (SEED compared with NOSEED) in the target area when compared with the same relative change in the untreated area. PIF is calculated as

$$\mathrm{PIF} = \frac{R_{S,T}}{R_{N,T}} \Big/ \frac{R_{S,U}}{R_{N,U}}. \quad (2)$$

Assuming the standard Z–R relationship form $R = aZ^b$, where a and b are constants, PIF is related to ZIP, as follows:

$$\begin{aligned}
\mathrm{ZIP} &= (10\log_{10}Z_{S,T} - 10\log_{10}Z_{N,T}) \\
&\quad - (10\log_{10}Z_{S,U} - 10\log_{10}Z_{N,U}) \\
&= 10\left[\log_{10}\left(\frac{Z_{S,T}}{Z_{N,T}}\right) - \log_{10}\left(\frac{Z_{S,U}}{Z_{N,U}}\right)\right] \\
&= 10\left[\log_{10}\left(\frac{R_{S,T}}{R_{N,T}}\right)^{1/b} - \log_{10}\left(\frac{R_{S,U}}{R_{N,U}}\right)^{1/b}\right] \\
&= \frac{10}{b}\log_{10}\left(\frac{R_{S,T}/R_{N,T}}{R_{S,U}/R_{N,U}}\right). \quad (3)
\end{aligned}$$

Combining (2) and (3),

$$\mathrm{PIF} = 10^{(b\times\mathrm{ZIP})/10}. \quad (4)$$

So the relationship between ZIP and PIF is independent of the coefficient a. The higher the exponent b is, the more sensitive the precipitation is to reflectivity. Experimental values for the exponent b for the WCR are $0.58 < b < 1.25$ (Geerts et al. 2010; Pokharel and Vali 2011). These studies are based on airborne snowfall rate estimates in winter storms in Wyoming. Theoretical work by Matrosov (2007) suggests $b = 1.25$ for W-band radars. For the MRR, experimental estimates for b in rain are $0.63 < b < 0.68$ (Tokay et al. 2009). Theoretical work by Matrosov (2007) specifically for snowfall suggests $b = 0.83$ for K-band radars. The Z–R relationship for nonattenuating frequency radars, which includes the X-band DOW at close range, has been explored in many studies in the last few decades. One commonly cited value for stratiform precipitation is $b = 0.71$ (e.g., Austin 1987), while for dry snow the published range is $0.5 < b < 0.67$ (Rasmussen et al. 2003). For simplicity, and because the uncertainty probably is larger than the difference in the quoted b values between the different radar frequencies, we use the value $b = 0.7$ for all three radars.

Profiles of ZIP and PIF for the three radars are shown in Fig. 12a. All three radars show positive ZIP values (and PIF > 1) near the surface, but they disagree about the magnitude: the WCR has the largest ZIP values, followed by the DOW and the MRR pair. The corresponding PIF values imply increases in the snowfall rate of 250%, 70%, and 10% for the WCR, the DOW, and the MRR pair, respectively, at their lowest data level. Differences are expected of course, since different SEED–NOSEED periods and different control–target areas are used for the three radars. While the ZIP values in the lowest 600 m (the average turbulent BL depth, according to WCR vertical velocity data) may be attributable to AgI seeding, that cannot be the case in the free troposphere, as it is very unlikely for AgI nuclei released at the ground to be carried above the BL. The positive ZIP values aloft indicate nonuniform temporal changes and actually reduce our confidence in the validity of the glaciogenic seeding attribution within the BL. The simple temporal change in the target area (not compared to that in a control area) actually is more consistent among the three radars (Fig. 12b).

5. Surface snow measurements

Snowfall was sampled by a Parsivel disdrometer and an ETI gauge at the Battle town site during this IOP. The Parsivel provides particle concentrations in 32 size bins and 32 fall-speed bins. The size bins range from 0.062 to 24.5 mm in diameter with 0.125-mm size intervals at smaller size and 3-mm intervals at larger size. The velocity bins range between 0.05 and 20.8 $\mathrm{m\,s}^{-1}$. The Parsivel's lower two size bins were found to be noisy so we did not use them.

The time series of the Parsivel snow size distribution, total snow particle concentration, and mean diameter all reveal a positive trend during the IOP (Fig. 13). The snow particle concentration increase only occurs in the second half (the last ~90 min) of SEED. Precipitation measured by the ETI gauge also shows an increase in precipitation rate during the second half of SEED (Fig. 13c). The DOW data confirm an increase in reflectivity near Battle Pass around 0000 UTC, but only one volume scan was collected after that (Table 1). It is possible that the AgI impact plume only reached Battle Pass around 0000 UTC; no wind shift occurred at Battle Pass or at

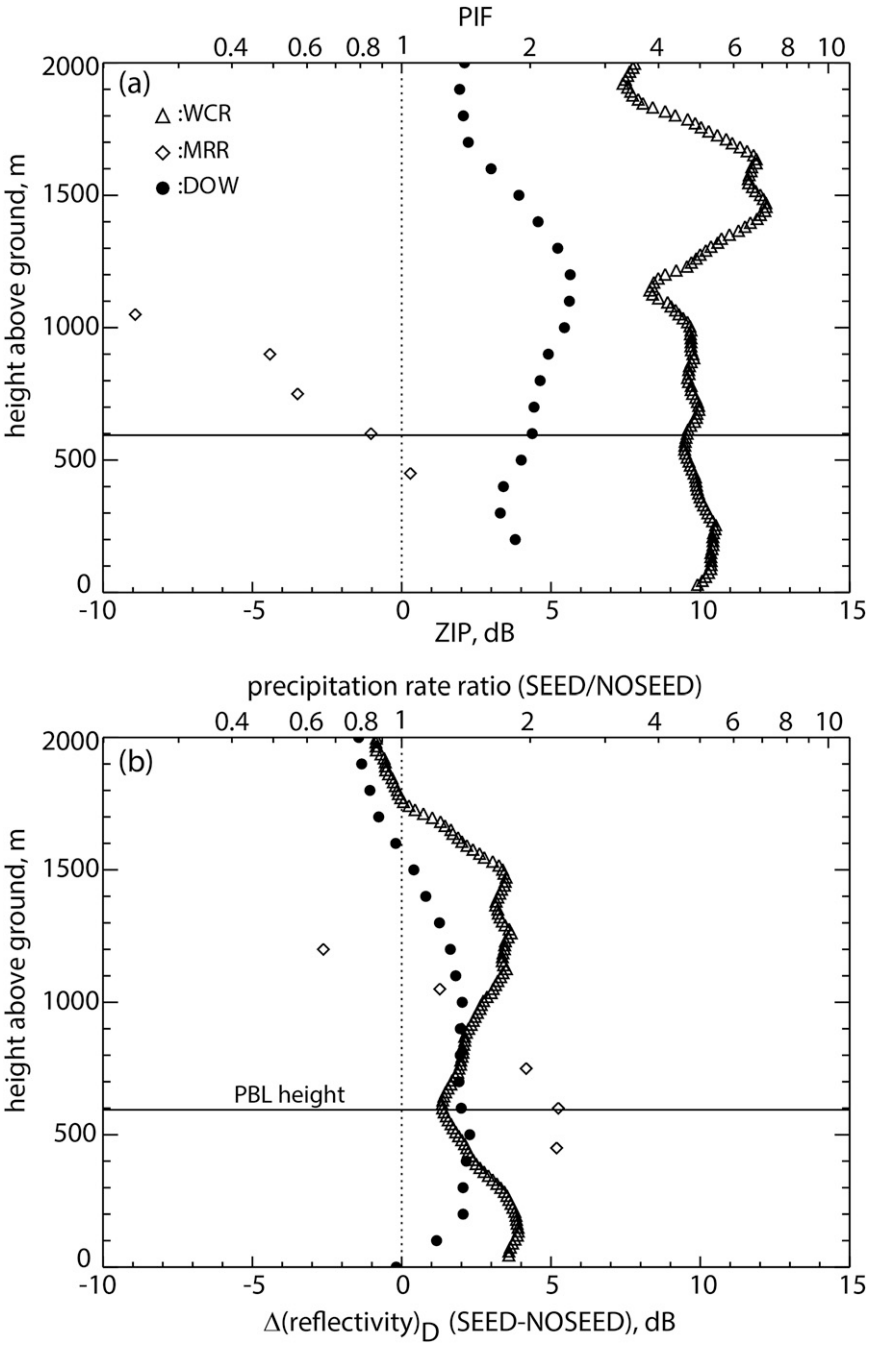

FIG. 12. Vertical profiles of seeding impact parameters for the WCR (triangles), MRR (diamonds), and DOW (circles) data, each with different control and target regions. (a) The seeding impact parameters ZIP and PIF (defined in the text). (b) Change in reflectivity and derived precipitation rate between SEED and NOSEED in the target region. The vertical dotted lines in (a) and (b) separate a positive effect to the right from a negative effect to the left. The horizontal solid line is the WCR-derived average PBL depth.

Dixon at that time. The particle concentration slowly tapers off during the post-SEED period (Fig. 13b), but the mean diameter remains large, consistent with steady snowfall according to the ETI gauge. The post-SEED period starts when the tail end of the AgI plume passes Battle Pass, assuming an advection speed equal to the sounding mean wind speed between the surface and Battle Pass. Clearly, AgI nuclei may linger behind in the BL.

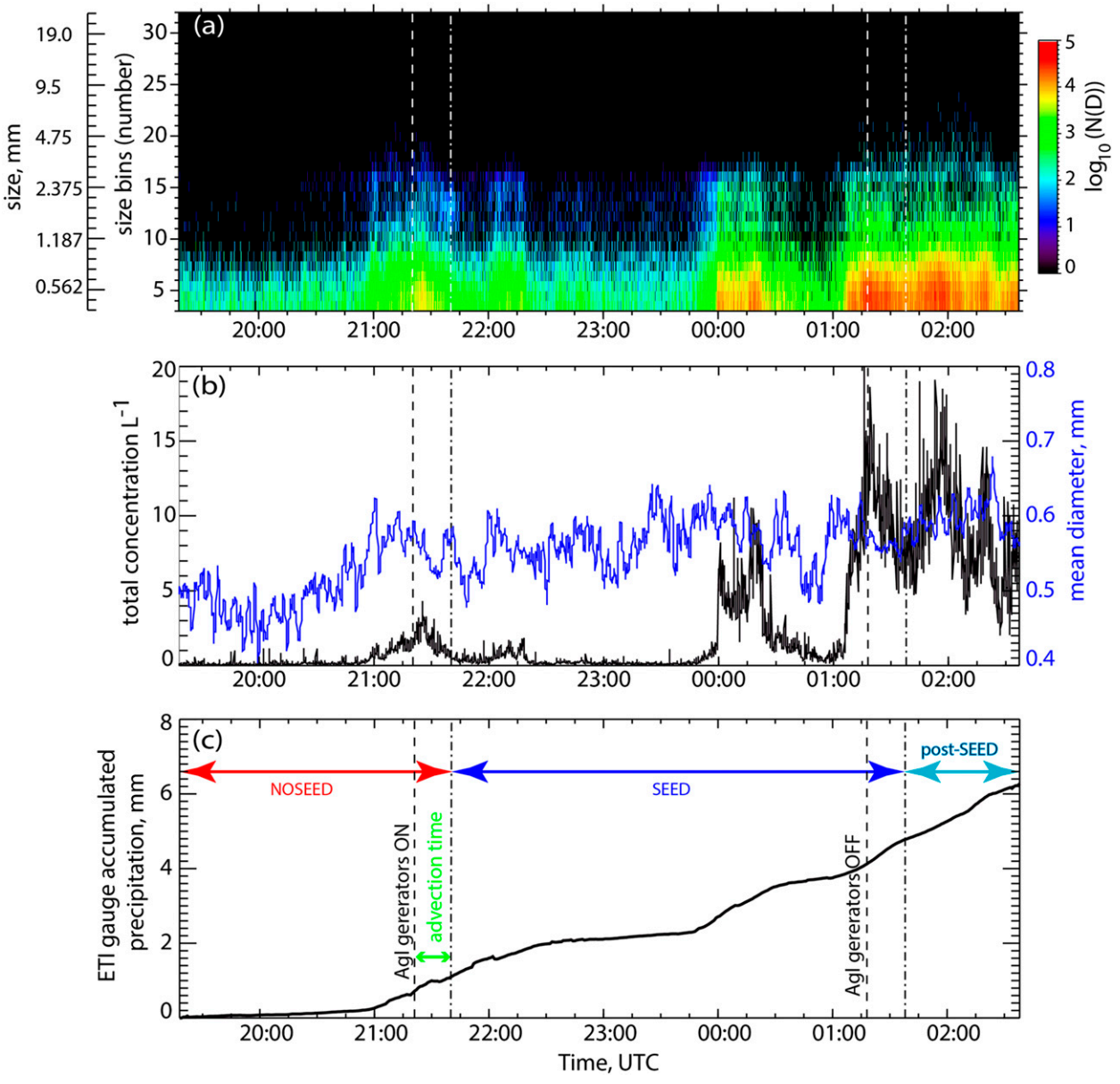

FIG. 13. Time series of snow measurements at Battle Pass. The vertical dashed lines in all panels mark the period of AgI nucleus dispersion from the ground-based generators, while the dashed–dotted lines delineate the NOSEED, SEED, and post-SEED periods at Battle Pass. (a) Parsivel disdrometer snow size distribution, (b) Parsivel total snow concentration and mean diameter, and (c) accumulated precipitation measured by ETI gauge.

The Parsivel frequency-by-diameter displays (FDDs) during NOSEED (Fig. 14a) and SEED (Fig. 14b) reveal the cumulative snow particle concentrations in different size bins. They confirm an increase in snow concentration in all size bins during SEED, mainly in the smaller size bins. This is more obvious in the difference FDD, which includes the mean concentration for different size particles during NOSEED and SEED (Fig. 14c). This change is significant, yet for an unknown reason it happened only in the second half of the Parsivel SEED period (Fig. 13), after the WCR and almost all of the DOW SEED periods had been completed. Unfortunately, no snow chemistry analysis from the Battle town site is available for this period.

6. Conclusions

This study analyzes data from three different radar systems, collected on 21 February 2012 near and downwind of a series of ground-based AgI generators in

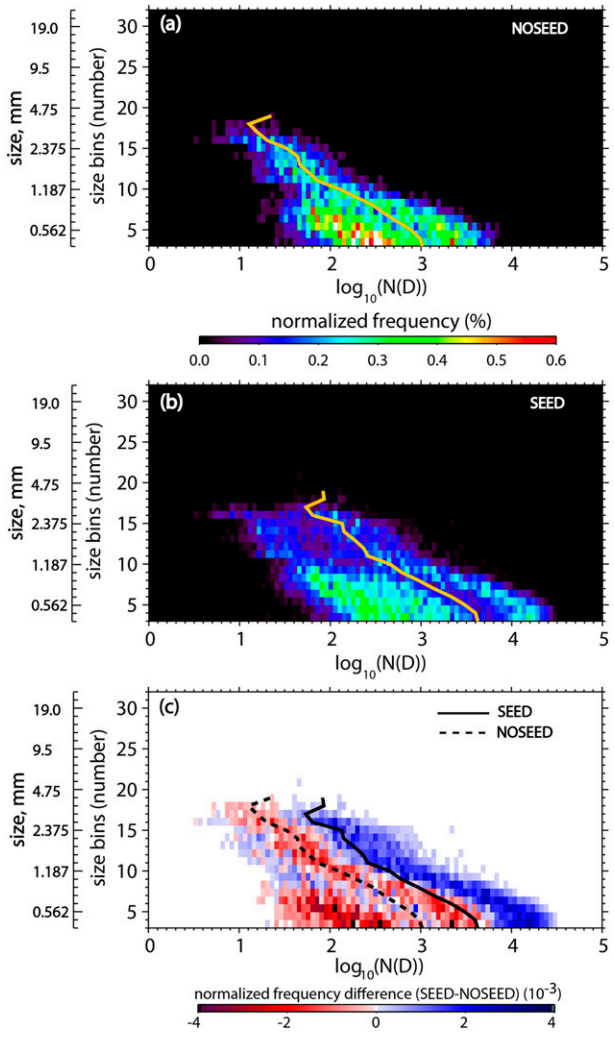

FIG. 14. FDD of snow particle concentration measured by the Parsivel at Battle Pass during the (a) NOSEED and (b) SEED periods. (c) The normalized frequency difference FDD between SEED and NOSEED. The solid lines in (a) and (b) show the average value; these lines are repeated as solid and dashed lines in (c).

the Sierra Madre in Wyoming. The radars include a profiling airborne W-band radar (WCR), a pair of profiling Ka-band MRRs, and an X-band scanning DOW. This study also analyzes Parsivel disdrometer data downstream of the generators, and is supported by a series of auxiliary measurements. The impact of glaciogenic seeding is studied by contrasting the seeding period (SEED) against the preceding untreated period (NOSEED). By design, the three radar systems allow comparisons between a control and a target region. The different radar systems are complementary in that they have different SEED/NOSEED periods and different target/control regions, although with overlaps. The key conclusions are as follow:

- The target storm contained substantial supercooled liquid water, evident from airborne lidar data, flight-level data, and a ground-based microwave radiometer. The storm was rather shallow, with a cloud-base (-top) temperature near −8°C (−22°C).
- The ambient conditions were remarkably steady during the IOP, although slight warming occurred. The storm depth decreased in all regions toward the end of the IOP. Two out of three radar systems indicate that the near-surface precipitation also decreased in their respective control regions near the IOP end.
- The three radar systems consistently point to an increase in low-level reflectivity in the target regions. The reflectivity impact factor, defined as the change in reflectivity (SEED − NOSEED) in the target region, relative to the same change in the control region, was positive near the surface for all three radar systems, although there was disagreement about the magnitude of this factor. The implication is that the near-surface snowfall rate increased in the target regions during AgI seeding relative to the proximity (untreated) storm evolution. Some caution is warranted about the attribution of this increase, as mountain-scale storm evolution cannot be assumed to be uniform.
- It is not certain that at least one of the AgI nuclei plumes (or AgI-impacted cloudy airstreams) reached the mountain pass site where the downwind MRR and the Parsivel disdrometer were located, although the wind (measured at various locations) was right. It is possible that the arrival of such a plume at the mountain pass site was delayed by ~2 h. Starting at that time and for the remainder of the SEED period, the concentration of snow particles of all sizes was significantly larger, without significant change in mean diameter.

In summary, this case study provides cumulative but not conclusive evidence that ground-based AgI seeding increased the near-surface snowfall rate over the Sierra Madre during the 21 February 2012 storm. Follow-up work includes a cloud-resolving large-eddy simulation of this case, with an inner-domain resolution of 100–300 m and an AgI cloud seeding parameterization (Xue et al. 2013).

Acknowledgments. The ASCII campaign is funded by National Science Foundation Grant AGS-1058426. This work also received funding from the Wyoming Water Development Commission and the U.S. Geological Survey, under the auspices of the University of Wyoming Water Research Program. The operation of the AgI generators, the upstream MRR, and the microwave radiometer was supported by the WWMPP, which is funded by the State of Wyoming and managed by Barry Lawrence. We thank Katja Friedrich and Dan Breed for

collecting and sharing MRR data at Battle Pass and Ladder Livestock ranch, respectively. We thank Katja Friedrich also for the disdrometer data collected at Battle Pass. We thank Arlen Huggins for the chemistry analysis of snow collected at Battle Pass. We used the NCAR-supported radar processing software Solo and Reorder.

REFERENCES

Austin, P. M., 1987: Relation between measured radar reflectivity and surface rainfall. *Mon. Wea. Rev.,* **115,** 1053–1070.

Breed, D., R. Rasmussen, C. Weeks, B. Boe, and T. Deshler, 2014: Evaluating winter orographic cloud seeding: Design of the Wyoming Weather Modification Pilot Project (WWMPP). *J. Appl. Meteor. Climatol.,* **53,** 282–299.

DeMott, P. J., 1997: Report to North Dakota Atmospheric Resource Board and Weather Modification Incorporated on tests of the ice nucleating ability of aerosols produced by the Lohse Airborne Generator. Dept. of Atmospheric Science, Colorado State University, Fort Collins, CO, 15 pp.

Deshler, T., D. W. Reynolds, and A. W. Huggins, 1990: Physical response of winter orographic clouds over the Sierra Nevada to airborne seeding using dry ice or silver iodide. *J. Appl. Meteor.,* **29,** 288–330.

Garstang, M., R. Bruintjes, R. Serafin, H. Orville, B. Boe, W. Cotton, and J. Warburton, 2005: Weather modification: Finding common ground. *Bull. Amer. Meteor. Soc.,* **86,** 647–655.

Geerts, B., Q. Miao, Y. Yang, R. Rasmussen, and D. Breed, 2010: An airborne profiling radar study of the impact of glaciogenic cloud seeding on snowfall from winter orographic clouds. *J. Atmos. Sci.,* **67,** 3286–3301.

——, ——, and ——, 2011: Boundary-layer turbulence and orographic precipitation growth in cold clouds: Evidence from profiling airborne radar data. *J. Atmos. Sci.,* **68,** 2344–2365.

——, and Coauthors, 2013: The AgI Seeding Cloud Impact Investigation (ASCII) campaign 2012: Overview and preliminary results. *J. Wea. Modif.,* **45,** 24–43.

Givati, A., and D. Rosenfeld, 2005: Separation between cloud-seeding and air-pollution effects. *J. Appl. Meteor.,* **44,** 1298–1314.

Grant, L. O., and R. E. Elliott, 1974: The cloud seeding temperature window. *J. Appl. Meteor.,* **13,** 355–363.

Holroyd, E. W., J. T. McPartland, and A. B. Super, 1988: Observation of silver iodide plumes over the Grand Mesa of Colorado. *J. Appl. Meteor.,* **27,** 1125–1144.

——, J. A. Heimbach, and A. B. Super, 1995: Observations and model simulation of AgI seeding within a winter storm over Utah's Wasatch Plateau. *J. Wea. Modif.,* **27,** 35–56.

Huggins, A. W., 1995: Mobile microwave radiometer observations: Spatial characteristics of supercooled cloud water and cloud seeding implications. *J. Appl. Meteor.,* **34,** 432–446.

——, 2007: Another wintertime cloud seeding case study with strong evidence of seeding effects. *J. Wea. Modif.,* **39,** 9–36.

Kristovich, D. A. R., B. Geerts, Q. Miao, L. Stoecker, and J. M. Ritzman, 2012: Airborne cloud radar and lidar observations of blowing snow during the ASCII project: A possible natural cloud seeding mechanism. *Proc. 19th Conf. on Mountain Meteorology,* Steamboat Springs CO, Amer. Meteor. Soc. [Available online at https://ams.confex.com/ams/15MountMet/webprogram/Paper210260.html.]

Li, Z., and R. L. Pitter, 1997: Numerical comparison of two ice crystal formation mechanisms on snowfall enhancement from ground-based aerosol generators. *J. Appl. Meteor.,* **36,** 70–85.

Löffler-Mang, M., and J. Joss, 2000: An optical disdrometer for measuring size and velocity of hydrometeors. *J. Atmos. Oceanic Technol.,* **17,** 130–139.

——, and U. Blahak, 2001: Estimation of the equivalent radar reflectivity factor from measured snow size spectra. *J. Appl. Meteor.,* **40,** 843–849.

Maahn, M., and P. Kollias, 2012: Improved Micro Rain Radar snow measurements using Doppler spectra post-processing. *Atmos. Meas. Tech.,* **5,** 2661–2673.

Matrosov, S. Y., 2007: Modeling backscatter properties of snowfall at millimeter wavelengths. *J. Atmos. Sci.,* **64,** 1727–1736.

——, C. Campbell, D. Kingsmill, and E. Sukovich, 2009: Assessing snowfall rates from X-band radar reflectivity measurements. *J. Atmos. Oceanic Technol.,* **26,** 2324–2339.

Morrison, A. E., S. T. Siems, and M. J. Manton, 2013: On a natural environment for glaciogenic cloud seeding. *J. Appl. Meteor. Climatol.,* **52,** 1097–1104.

National Research Council, 2003: *Critical Issues in Weather Modification Research.* National Academy Press, 123 pp.

Pokharel, B., and G. Vali, 2011: Evaluation of collocated measurements of radar reflectivity and particle sizes in ice clouds. *J. Appl. Meteor. Climatol.,* **50,** 2104–2119.

Rasmussen, R., M. Dixon, S. Vasiloff, F. Hage, S. Knight, J. Vivekanandan, and M. Xu, 2003: Snow nowcasting using a real-time correlation of radar reflectivity with snow gauge accumulation. *J. Appl. Meteor.,* **42,** 20–36.

Rogers, D. C., and G. Vali, 1987: Ice crystal production by mountain surfaces. *J. Climate Appl. Meteor.,* **26,** 1152–1168.

Saleeby, S. M., W. R. Cotton, D. Lowenthal, R. D. Borys, and M. A. Wetzel, 2009: Influence of cloud condensation nuclei on orographic snowfall. *J. Appl. Meteor. Climatol.,* **48,** 903–922.

Schaefer, V. J., 1946: The production of ice crystals in a cloud of supercooled water droplets. *Science,* **104,** 457–459.

Super, A. B., 1999: Summary of the NOAA/Utah Atmospheric Modification Program: 1990–1998. *J. Wea. Modif.,* **31,** 51–75.

——, and B. A. Boe, 1988: Microphysical effects of wintertime cloud seeding with silver iodide over the Rocky Mountains. Part III: Observations over the Grand Mesa, Colorado. *J. Appl. Meteor.,* **27,** 1166–1182.

——, and J. A. Heimbach, 1988: Microphysical effects of wintertime cloud seeding with silver iodide over the Rocky Mountains. Part II: Observations over the Bridger Range, Montana. *J. Appl. Meteor.,* **27,** 1152–1165.

——, B. A. Boe, J. A. Heimbach, J. T. McPartland, and G. Langer, 2010: Comparison of silver iodide outputs from two different generators and solutions measured by acoustic ice nucleus counters. *J. Wea. Modif.,* **42,** 49–60.

Tokay, A., P. Hartmann, A. Battaglia, K. S. Gage, W. L. Clark, and C. R. Williams, 2009: A field study of reflectivity and *Z–R* relations using vertically pointing radars and disdrometers. *J. Atmos. Oceanic Technol.,* **26,** 1120–1134.

Vali, G., D. Leon, and J. R. Snider, 2012: Ground-layer snow clouds. *Quart. J. Roy. Meteor. Soc.,* **138,** 1507–1525.

Vonnegut, B., 1947: The nucleation of ice formation by silver iodide. *J. Appl. Phys.,* **18,** 593–595.

Wang, Z., and Coauthors, 2012: Single aircraft integration of remote sensing and in situ sampling for the study of cloud microphysics and dynamics. *Bull. Amer. Meteor. Soc.,* **93,** 653–668.

Xue, L., S. Tessendorf, E. Nelson, R. Rasmussen, D. Breed, S. Parkinson, P. Holbrook, and D. Blestrud, 2013: Implementation

of a silver iodide cloud seeding parameterization in WRF. Part II: 3D simulations of actual seeding events and sensitivity tests. *J. Appl. Meteor. Climatol.,* **52,** 1458–1476.

Yuter, S. E., and R. A. Houze Jr., 1995: Three-dimensional kinematic and microphysical evolution of Florida cumulonimbus. Part II: Frequency distributions of vertical velocity, reflectivity, and differential reflectivity. *Mon. Wea. Rev.,* **123,** 1941–1963.

——, D. E. Kingsmill, L. B. Nance, and M. Löffler-Mang, 2006: Observations of precipitation size and fall speed characteristics within coexisting rain and wet snow. *J. Appl. Meteor. Climatol.,* **45,** 1450–1464.

Zipori, A., D. Rosenfeld, J. Shpund, D. M. Steinberg, and Y. Erel, 2012: Targeting and impacts of AgI cloud seeding based on rain chemical composition and cloud top phase characterization. *Atmos. Res.,* **114–115,** 119–130.